Phase diagrams and thermodynamics of rare-earth-doped zirconia ceramics*

Chong Wang, Matvei Zinkevich‡, and Fritz Aldinger

Max-Planck-Institut für Metallforschung and Institut für Nichtmetallische Anorganische Materialien, Universität Stuttgart, Heisenbergstraße 3, D-70569 Stuttgart, Germany

Abstract: Results of the comprehensive experimental and computational phase studies of the systems ZrO_2–$REO_{1.5}$ (RE = La, Nd, Sm, Gd, Dy, Yb) are summarized. Various experimental techniques, X-ray diffraction (XRD), scanning electron microscopy (SEM), electron probe microanalysis (EPMA), transmission electron microscopy (TEM), differential thermal analysis (DTA), and high-temperature calorimetry are employed to study the phase transformation, phase equilibria between 1400 and 1700 °C, heat content and heat capacity of the materials. A lot of contradictions in the literature are resolved, and the phase diagrams are reconstructed. Based on the experimental data obtained in this work and literature, the systems ZrO_2–$REO_{1.5}$ are thermodynamically optimized using the CALPHAD (CALculation of PHase Diagram) approach. Most of the experimental data are well reproduced. Based on the present experiments and calculations, some clear characteristic evolutions with the change of the ionic radius of doping element RE^{+3} can be concluded.

Keywords: ceramics; rare-earth-doped; phase diagram; CALPHAD; zirconia.

INTRODUCTION

Nowadays, the design of a new generation of thermal barrier coatings (TBCs) for high-temperature gas turbine engines is increasingly promoted. The crucial ZrO_2-based TBC or "top coat" plays an important role for improving the performance and lifetime of gas turbine engines, by creating a large temperature gradient (100–300 °C) from the surface of the layer of the TBC to the coated alloy components. Such benefit allows one to increase the hot gas temperature around the engines and improve the efficiency, without change of the Ni-based superalloy components.

Worldwide, a lot of effort has been put into the development of alternative ceramics for TBCs other than state-of-the-art YSZ (yttria-stabilized zirconia), aiming to lower thermal conductivity and/or to improve high-temperature performance and durability [1], so that larger temperature gradients can be established through the TBC without excessive augmentation of its thickness. Co-doping of YSZ by rare earths (REs) such as Gd is of interest in thermal barrier systems because of concomitant benefits to the thermal insulating efficiency [2,3]. Some RE zirconates have been proposed to reduce the thermal conductivity of TBCs by as much as 30 % of current levels without the change of the thermal stability [4,5]. At the same time, the TBC/Al_2O_3 (thermally grown oxide, TGO) interface can maintain good thermochemical compatibility and stability at high temperatures without losing the reliability of

---

TBCs. Especially, the pyrochlore phases in some systems of RE oxides combined with ZrO_2 are paid much more attention in recent years because they combine lower thermal conductivity with enhanced microstructural stability upon high-temperature exposure [1,5–7].

Although there are numerous literature works on zirconia, most of them are concentrated on the materials properties. Phase equilibria or phase transformation studies mainly concern the ZrO_2–Y_2O_3, ZrO_2–CeO_2, ZrO_2–CaO, and ZrO_2–MgO systems. As for the ZrO_2–RE_2O_3 systems except RE = Y, only very limited phase equilibria and thermodynamic investigations are available in the literature, despite the fact that the importance of such systems has already been realized. Also, the martensitic transformation temperatures are affected by many factors such as particle size, impurities, stress, and thermal history of materials, the literature data present large discrepancies, and no quantitative analysis has been done yet on how these factors can affect the transformation temperatures.

In this paper, results of the comprehensive experimental and computational phase studies of the systems ZrO_2–$REO_{1.5}$ (RE = La, Nd, Sm, Gd, Dy, Yb) are summarized. The detailed description of experimental results and thermodynamic modeling can be found in the thesis work [8].

PHASE TRANSFORMATIONS IN ZrO_2-BASED SYSTEMS AND THEIR IMPLICATIONS FOR THERMAL BARRIER COATINGS

Phase transformation phenomena in doped zirconia

It is well known that the phase transformation behavior in doped ZrO_2 presents large complexity. There are three structural modifications for the pure ZrO_2 at ambient pressure: the cubic structure with the fluorite type ($Fd\bar{3}m$) at high temperatures, the tetragonal structure ($P4_2/nmc$) at intermediate temperatures, and the monoclinic structure ($P2_1/c$) at low temperatures. Many experimental studies confirmed that the monoclinic $\leftrightarrow$ tetragonal phase transformation is of displacive martensitic type [9].

The solubility of REs in the monoclinic ZrO_2 phase is negligible, while the tetragonal phase can dissolve considerable amounts of RE elements depending on the radius of cations. The tetragonal ZrO_2 phase cannot be stabilized to low temperature due to the diffusionless martensitic transformation. Since about 8 % volume change is associated with this transformation, cracks can form at the grain boundaries, which are harmful to the materials.

The tetragonal $\leftrightarrow$ monoclinic athermal phase transformation occurs martensitically with a temperature hysteresis loop near 1373 K [10] for pure ZrO_2. The hysteresis loop extends about 200 K for ZrO_2. Generally, the transformation temperatures on heating and cooling are referred to as A_s (starting) and A_f (finishing), and as M_s (starting) and M_f (finishing). For thermodynamic studies, the equilibrium temperature (T_0, where the Gibbs energies of monoclinic and tetragonal phases are identical) is undoubtedly important. Due to the experimental difficulty in the direct measurement of the T_0 temperature, it is customary to calculate it empirically by the equation [11]

$$T_0 = \frac{A_s + M_s}{2} \tag{1}$$

or

$$T_0 = \frac{A_f + M_f}{2} \tag{2}$$

The high-temperature cubic fluorite-type structure can be stabilized to lower temperatures by doping with certain amounts of RE elements, so that the destructive tetragonal $\leftrightarrow$ monoclinic transition can be avoided. Nevertheless, in some composition range, even the cubic phase is not quenchable due to a diffusionless transformation from cubic to another kind of tetragonal phase T' [12,13]. Such diffusionless transformation occurs near the stable cubic + tetragonal two-phase region, within a certain temperature hysteresis during heating and cooling. Unlike the equilibrium tetragonal phase, the T' phase is

kinetically non-transformable into the equilibrium phase assemblage at low temperatures due to its smaller axis ratio c/a than that of equilibrium tetragonal phase, although it is thermodynamically metastable.

Implications for the thermal barrier coatings

Due to the destructive tetragonal-to-monoclinic phase transition, the composition of the TBCs must satisfy the demand to avoid this transformation. The TBCs are often partially stabilized zirconia, i.e., the metastable supersaturated T' phase, which is the most preferred TBC material of practical interest because of its higher cyclic lives [1]. However, it can transform into the stable tetragonal and fluorite phases during the long-term thermal cycling, and thus brings the risk of failure due to the destructive martensitic transformation. To select the composition and thermal cycling temperature range (operating temperature limits), it is very important to understand the equilibrium phase diagrams, so that the formation of stable tetragonal phase can be avoided, and the appropriate operating temperature limits can be determined to prevent the destructive transformation. In a recent study, it was found that the YSZ TBC partly transforms into stable tetragonal phase at 1425 °C [14]. It is reasonable to believe that the upper temperature limits are different for the materials with different compositions or doping elements according to the phase diagrams of different systems. Moreover, when the martensitic transformation temperatures are well determined against the doping elements, it is possible to control the thermal cycling temperature range to avoid the transformation.

A possible failure of the thermal barrier system occurs at the TBC/TGO interface, if the TGO is not thermodynamically stable and reacts with the TBC. As an example, the pyrochlore phases of some ZrO_2–RE_2O_3 (RE = rare earth element) systems are very promising TBC materials for their lower thermal conductivity and high-temperature stability, however, they react with Al_2O_3. The phase diagram calculations can give the answer if the TBC reacts with the TGO. Furthermore, the limits of doping and the temperature range in which the TBC can stably coexist with the TGO can be determined [15]. For example, compositions with more than ~32 mol % $GdO_{1.5}$ are not thermochemically compatible with the underlying alumina layer in the coating system [7,16] and tend to form interphases at high temperature, with significantly active kinetics at ~1100 °C and above [7]. An approach to circumvent the problem is to add an interlayer of YSZ between $Gd_2Zr_2O_7$ and the underlying alumina [1]. It is undoubted that precise phase diagrams and thermodynamic data are very helpful tools to study the interfacial stabilities in the thermal barrier system.

EXPERIMENTAL PROCEDURES

Sample preparation

The zirconium acetate solution, $Zr(CH_3COO)_4$ (99.99 %, Sigma–Aldrich), rare earth nitrate hydrate, $RE(NO_3)_3 \cdot xH_2O$ (99.99 %, Alfa Aesar) are adopted as the starting chemicals. The $RE(NO_3)_3 \cdot xH_2O$ was dissolved in the water as the first step. After the determination of the oxide yield of different solutions, they were mixed according to the given ratios. Thus obtained precursor solution was dropped from the buret at a low speed (around 1 ml min^{-1}) into a big beaker containing about 500 ml of deionized water, while maintaining the pH value above 9.0 by adding ammonium hydrate. The precipitation occurred during dropping and stirring. The precipitate was then filtered and dried at 75 °C. Finally, the white powder was obtained after pyrolysis of the dried precipitate at 700 °C for 3 h or 1000 °C for 1 h in air.

Sample treatment and characterization

The pyrolyzed powder was isostatically pressed into cylindrical pellets and sintered in air at temperatures ranging from 1400 to 1700 °C to obtain the equilibrium microstructure (Pt-crucible, heating and cooling rate of 10 K min^{-1}). The duration of heat treatments was 10 days at 1400 °C, 5 days at 1500 °C, 3 days at 1600 °C, and 36 h at 1700 °C. The samples were then analyzed by X-ray diffraction (XRD), scanning electron microscopy (SEM), electron probe microanalysis (EPMA), transmission electron microscopy (TEM), differential thermal analysis (DTA), and high-temperature calorimetry.

The XRD patterns of powdered specimens were recorded on Siemens diffractometer D5000 (CuKα_1 radiation, $\lambda = 0.15406$ nm, 2θ range 10–80°, 2θ step of 0.016°, time per step 0.2 s). Precise measurements of lattice parameters were carried out using silicon or alumina powder as internal standard.

The microstructures of sintered samples were examined by SEM (Zeiss DSM 982 GEMINI operating at 20 kV and 10 nA) and the energy dispersive X-ray spectroscopy (EDX, Oxford-Instrument ISIS 300) was employed to obtain the compositions of phases (± 1 mol % $REO_{1.5}$) in equilibrium state. Furthermore, the electronic probe microanalyzer (EPMA, SX-100, Cameca) was also employed for the precise composition analysis.

The ZrO_2-rich samples were studied by DTA up to 1700 °C (Bähr, heating and cooling rate 5 K/min, Al_2O_3 crucible). The uncertainty of the measurements is estimated to be ± 5 K.

OVERVIEW OF PHASES AND THERMODYNAMIC MODELS

The compound energy formalism developed by M. Hillert et al. [17] can be applied to most of the solution phases, which have separate crystallographic sublattices. It is called formalism because it includes a large variety of thermodynamic models. It assumes that in crystals different atomic species occupy separate (the stoichiometric compounds) or same sublattices (the phases with composition range). A certain sublattice can be occupied by the intrinsic atoms, anti-site atoms, interstitial atoms, vacancies, and electrons. The compound energy formalism can be thought of as the substitutional model applied for the case of a phase with two or more sublattices. This generalized model can be used to describe different solution phases with substitutional and intersititial species, charged species, ordering behavior, etc. The construction of the sublattices should be exactly based on the structure information of phases, so that the model has a physical meaning.

The model for a solution phase can be expressed with the formula $(A,B,\ldots)_k (C,D,\ldots)_l(\ldots)_{\ldots}$, in which A, B, C, D,... are the constituents, and k, l, … are called stoichiometric coefficients. The division on sublattices is made according to the phase structures, and in principle there are no limitations on the numbers of sublattices. The Gibbs energy function of generalized model is given by

$$G_m = \sum \prod y_J^S \, {}^0G_{\text{end}} + RT \sum \sum n^S y_J^S \ln(y_J^S) + {}^E G_m \tag{3}$$

in which n^S is stoichiometric coefficient of sublattice S, and y_J^S is the site fraction of constituent J in the sublattice S. ${}^0G_{\text{end}}$ is the Gibbs energy of end members which are the stoichiometric compounds formed by the constituents when each sublattice is occupied by only one species, e.g., $A_kC_l\ldots$. The excess Gibbs energy ${}^E G_m$ is expressed by

$$^E G_m = \prod y_J^S \sum y_B^t L_{A,B:C:D\ldots} + \prod y_J^S \sum \sum y_B^t y_D^u L_{A,B:C,D:E\ldots} + \ldots \tag{4}$$

where the commas in the subscripts separate different constituents in the same sublattice, and the colons separate the species in different sublattices. In the first group of terms, the interaction parameter $L_{A,B:C:D\ldots}$ describes the interactions in a certain sublattice while each of the other sublattices is only occupied by a single constituent. In the second group of terms, the interaction parameter $L_{A,B:C,D:E\ldots}$ describes the interactions occur in two sublattices at the same time while each of the other sublattices is

only occupied by a single constituent, and this interaction parameter is called "reciprocal parameter". All these interaction parameters can be expanded as the Redlich–Kister polynomials [18].

The liquid phase of ZrO_2–$REO_{1.5}$ system is also described with the two-sublattice model for ionic liquids [17] $(RE^{+3}, Zr^{+4})_P(O^{-2})_Q$ but without vacancies in the anion sublattice. Three kinds of ZrO_2-based solid solutions with cubic fluorite-type, tetragonal, and monoclinic structures are treated with the same model $(RE^{+3}, Zr^{+4})_2(O^{-2}, Va)_4$.

In the RE_2O_3-rich region, there are five polymorphic structures named A, B, C, H, and X [19]. In the C-type structure all cations are in six-fold coordination, while in the B-type structure some of them are surrounded by seven oxygen anions. This seven-fold coordination is a characteristic feature of the A-type structure. Both the H- and X-type structures are built from octahedra, which are distorted in the former case. At normal conditions, hexagonal A-form is the stable structure for RE = La, Ce, Pr, Nd, while Sm_2O_3, Eu_2O_3, and Gd_2O_3 may exist in both monoclinic B- and cubic C-form. The C-type structure is characteristic for RE = Tb, Dy, Ho, Er, Tm, Yb, Lu, Y, and Sc. The A-, B-, or C-RE_2O_3, except Lu_2O_3 and Sc_2O_3, transform into hexagonal H-phase at sufficiently high temperatures. The latter converts into high-temperature cubic X-RE_2O_3 for RE = La–Dy before the melting occurs. Such phases with solubility range are described by the three-sublattice model $(RE^{+3}, Zr^{+4})_2(O^{-2})_3(O^{-2}, Va)_1$.

Two kinds of ordered superstructures of the fluorite phase are known to occur in the ZrO_2–$REO_{1.5}$ systems at low temperatures: the pyrochlore phase and the δ phase. The general formula of the pyrochlore structure can be written as $A_2B_2O_6O'$. There are four crystallographically unique atom positions for the stoichiometric phase, and the space group is $Fd\bar{3}m$. The pyrochlore structure of stoichiometric $A_2B_2O_7$ can be derived from the fluorite structure by doubling the fluorite cell edge, placing the large A^{+3} ions at *16d* site, the smaller B^{+4} ions at *16c*, and the O^{-2} ions at *48f* and *8b*, leaving the fluorite position *8a* vacant. The A^{+3} cations are eight-fold coordinated with six *48f* oxygen atoms (O1) and two *8b* oxygen atoms (O2), and the B^{+4} cations are coordinated with six *48f* oxygen atoms, while the O1 anions in *48f* site are coordinated with two A^{+3} and two B^{+4} cations, and O2 anions in *8b* site are coordinated with four A^{+3} cations [20,21]. The substitution between A^{+3} and B^{+4} or introducing point defects into the pyrochlore-type structure (vacancies or interstitials) resulting in formation of the non-stoichiometric phases $A_{2-x}B_{2+x}O_{7+0.5x}$. The pyrochlore phase is described by five-sublattice model, i.e., $(Zr^{+4}, RE^{+3})_2(RE^{+3}, Zr^{+4})_2(O^{-2}, Va)_6(O^{-2})_1(Va, O^{-2})_1$, in which the fourth sublattice is fully occupied by oxygen. Additionally, the splitting model $(Zr^{+4}, RE^{+3})_2(RE^{+3}, Zr^{+4})_2(O^{-2}, Va)_8$ was used to describe the second-order transition in the ZrO_2–$GdO_{1.5}$ system.

The δ phase is observed when the ionic radius of the doping element RE^{+3} is smaller than that of Dy^{+3} [22]. The crystal structure of this phase can be derived from the defective fluorite structure by the ordering of oxygen vacancies to produce a rhombohedral cell. There are two different cation positions: (1) the single site at the origin which is octahedrally coordinated with anions, and (2) the six equivalent sites which are coordinated by anions on seven of the eight vertices of a slightly distorted cube. For the ideally ordered δ phase, the position *3a* is fully occupied by Zr^{+4}, and the other cationic sites *18f* are occupied by RE^{+3} ions and the residual Zr^{+4} ions, while the oxygen ions occupy two anion *18f* positions and the anion vacancies are on the position *6c* [22,23]. Based on crystal structure information, in this work the δ phase is described with the four-sublattice model $(Zr^{+4})_1(RE^{+3}, Zr^{+4})_6(O^{-2}, Va)_{12}(Va, O^{-2})_2$.

The following abbreviations are used throughout this paper: L for the liquid; M, T, and F for the solid solutions isostructural with the monoclinic, tetragonal, and cubic ZrO_2; P and δ for the intermediate pyrochlore and δ ($RE_4Zr_3O_{12}$) phases; and C, B, A, H, X for the solid solutions isostructural with the corresponding polymorph of the RE sesquioxides.

PHASE DIAGRAMS

ZrO$_2$–LaO$_{1.5}$ system

The high-temperature fluorite phase in the the ZrO$_2$–LaO$_{1.5}$ system cannot be stabilized to low temperature by the doping of La, and the solubility of La in the tetragonal phase is not clear. The pyrochlore phase melts congruently, but the homogeneity range is not clear yet due to the scattered experimental data. The high-temperature invariant reactions are well determined. The existence of the C$_2$ phase reported by [24,25] was not confirmed by other works, and could be the fluorite phase, by taking account of the similarities of many ZrO$_2$–REO$_{1.5}$ systems.

The calculated ZrO$_2$–LaO$_{1.5}$ phase diagram is shown in Fig. 1. The calculated eutectic points for the reactions L ↔ F + P and L ↔ F + X-La$_2$O$_3$ are 2529 K (41.6 mol % LaO$_{1.5}$) and 2288 K (77.7 mol % LaO$_{1.5}$) respectively, which fall well among the results of [24–26]. The calculated liquidus presents some deviation from the experimental data of [25], because the work of [26] was considered in the optimization. Moreover, the sharp liquidus reported by [25] was also questioned by the previous review on this system [27]. For the melting point of the pyrochlore phase, the result of the present work (2556 K) is closer to the data of [25] than that of [26]. The results of [26] are not given a higher weight for assessment because no detailed information on the measurements is given. However, in a parallel work on the ZrO$_2$–LaO$_{1.5}$–AlO$_{1.5}$ system, it has been proven that the optimized phase diagram without taking account of the data of [26] will have a worse agreement with the liquidus projection of the ternary phase diagram. In fact, because the experimental uncertainty of 100 K at such temperatures is normal for many systems, the present calculations are thought to be reasonable.
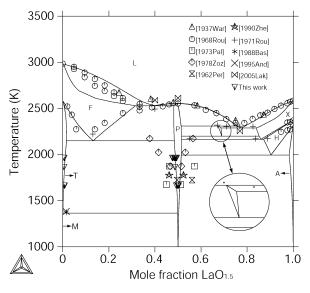

Fig. 1 Calculated ZrO$_2$–LaO$_{1.5}$ phase diagram together with experimental data.

In the LaO$_{1.5}$-rich region, the calculated data of the reactions L + P ↔ F (2309 K, 75.6 mol % LaO$_{1.5}$), F ↔ P + X-La$_2$O$_3$ (2192 K, 69.1 mol % LaO$_{1.5}$) and X-La$_2$O$_3$ ↔ P + H-La$_2$O$_3$ (2165 K, 86 mol % LaO$_{1.5}$) show reasonable agreements with the experimental results obtained by Rouanet [25], while the compositions of the solid phases could not be well fitted, because it was already accepted that the homogeneity range of the pyrochlore phase is not so wide, and the composition of X-La$_2$O$_3$ phase

reported by [25] is also less reliable for their experimental difficulties at high temperatures. For the reaction H-La$_2$O$_3$ ↔ P + A-La$_2$O$_3$, the present calculation reveals a value of 1994 K.

At the ZrO$_2$-rich side of the diagram, the experimental data on the P + T equilibrium obtained in this work are well reproduced. However, the calculated temperature of the invariant reaction F ↔ P + T cannot be fitted to value as high as 2223 K reported by [25], unless a very positive enthalpy of formation of the fluorite phase is used. The calculated enthalpy of formation of the fluorite phase with respect to the monoclinic ZrO$_2$ and A-type LaO$_{1.5}$ is –862 J.mol^{-1}. A much more positive enthalpy of formation will make the fluorite only stable at high temperatures. Owing to the similarities of ZrO$_2$–REO$_{1.5}$ systems, it is reasonable to assume that before ordering occurs, the fluorite phase is always stable at room temperature. The calculated temperature of the reaction T ↔ P + M is 1363 K, which is only 4 K lower than the T_0 temperature for pure ZrO$_2$. Moreover, the calculated composition of the tetragonal phase for this reaction is only 0.13 mol % LaO$_{1.5}$ which is consistent with present experimental result. The higher value 1.5 mol % LaO$_{1.5}$ reported by [10,28] is thought to be the composition at a nonequilibrium state.

ZrO$_2$–NdO$_{1.5}$ system

The calculated ZrO$_2$–NdO$_{1.5}$ phase diagram is presented in Fig. 2, compared with the experimental data. Due to a wide tetragonal + fluorite two-phase region, the fluorite phase cannot be completely stabilized to low temperature. It decomposes into the tetragonal and pyrochlore phases at 1487 K and 23.4 mol % NdO$_{1.5}$ according to the calculation. The calculated invariant reaction T ↔ M + P occurs at 1326 K and 1.0 mol % NdO$_{1.5}$, which is consistent with the composition reported by [10]. However, the temperature (1153 K) suggested for the reaction by [10] is much lower, and is actually the temperature of the martensitic transformation, which is not corresponding to this invariant reaction. The calculated T_0 line for the monoclinic and tetragonal phases (Fig. 3) reproduces well the data of [10,29]. For the diffusionless fluorite-to-tetragonal transition, the calculation gives the prediction that the T' phase can be only obtained for compositions less than 12 mol % NdO$_{1.5}$.
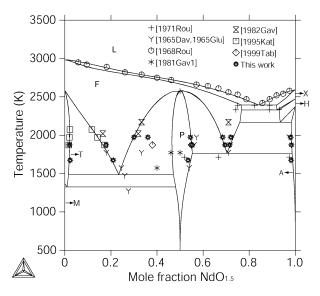

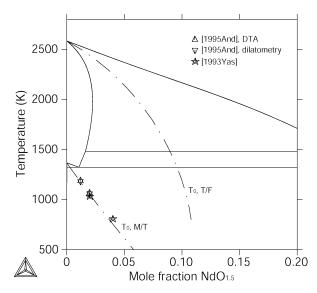**Fig. 2** Calculated ZrO$_2$–NdO$_{1.5}$ phase diagram compared with the experimental data.

Fig. 3 Calculated ZrO_2–$NdO_{1.5}$ partial phase diagram, and T_0 lines for monoclinic + tetragonal and tetragonal + fluorite equilibria together with experimental data.

The experimental data on the fluorite + pyrochlore phase equilibrium are reproduced well within the experimental limits. To fit the phase boundary of the fluorite phase at the $NdO_{1.5}$-rich side, the congruent transition temperature has to be elevated by 11 K with respect to 2573 K estimated by [25]. Compared to the ZrO_2–$LaO_{1.5}$ system, the homogeneity range of the pyrochlore phase in the ZrO_2–$NdO_{1.5}$ system is considerably larger. The temperature of the invariant reaction F ↔ P + A-Nd_2O_3 is calculated to be 1763 K, which is 50 K higher than the result reported in [25], while the calculated compositions of the fluorite and pyrochlore phases show deviation with the experimental data [25] within 5 mol % $NdO_{1.5}$. At high temperatures, the calculated invariant reactions L ↔ F + X-Nd_2O_3 (2393 K, L: 84.1 mol % $NdO_{1.5}$) and X-Nd_2O_3 ↔ F + H-Nd_2O_3 (2330 K, X: 92.1 mol % $NdO_{1.5}$) are considerably consistent with those data reported by Rouanet [25] within the limits of uncertainties. The reaction H-Nd_2O_3 ↔ F + A-Nd_2O_3 is predicted at 2169 K.

ZrO_2–$SmO_{1.5}$ system

The calculated ZrO_2–$SmO_{1.5}$ phase diagram is shown in Fig. 4, together with the experimental data. The phase equilibria data obtained in this work and those of [25,30,31] are well reproduced. It can be seen in Fig. 4 that the calculated tetragonal + fluorite two-phase region is well consistent with the experimental data of this work and of [30]. Compared with the ZrO_2–$NdO_{1.5}$ system, this two-phase region of the ZrO_2–$SmO_{1.5}$ system is a little bit narrower. The calculated invariant reaction T ↔ M + F is 1315 K, at which temperature the solubility of $SmO_{1.5}$ in the tetragonal phase is only 1.3 mol %, and the homogeneity range of the monoclinic phase is negligible. Figure 5 shows the calculated ZrO_2-rich partial phase diagram including the calculated T_0 lines for the monoclinic + tetragonal and tetragonal + fluorite phase equilibria and experimental data. The results of [10,29] on the T_0 line of the former one are well reproduced.

The calculated pyrochlore + fluorite equilibrium fit the phase boundary data obtained in this work and [31], as well as the transformation temperature reported by [25]. Two invariant reactions involving the pyrochlore phase are calculated at 1103 K (F ↔ M + P) and 1505 K (F ↔ P + B-Sm_2O_3), respectively. At the $SmO_{1.5}$-rich side, the phases pyrochlore, B-Sm_2O_3 and C-Sm_2O_3 are in equilibrium at low
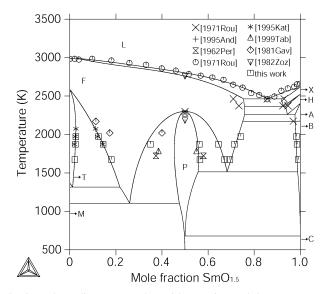
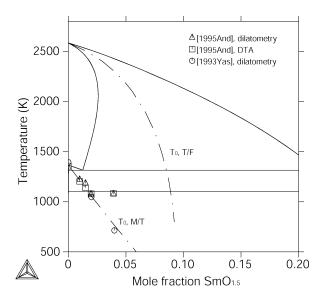**Fig. 4** Calculated ZrO_2–$SmO_{1.5}$ phase diagram together with experimental data.

Fig. 5 Calculated ZrO_2–$SmO_{1.5}$ partial phase diagram together with the calculated T_0 lines for the monoclinic + tetragonal and tetragonal + fluorite phase equilibria and experimental data.

temperatures. Since it is not possible to equilibrate samples at such conditions, there is no experimental evidence for this, where the solubility range of C-Sm_2O_3 phase is neglected.

The experimental data obtained in this work are taken into account to optimize the phase boundaries of the fluorite + B-Sm_2O_3 phase equilibrium. A good agreement with the calculation is obtained. This agreement makes the calculations get less consistency with the experimental compositions of the fluorite phase for invariant reactions reported by [25] at higher temperatures. However, owing to the large uncertainties of the HTXRD data of [25], present calculations are thought to be more reasonable by fitting the reliable phase boundary data. All the reported temperatures of the invariant reactions are

reproduced well within the limits of experimental uncertainties. The temperature of the reaction $H\text{-}Sm_2O_3 \leftrightarrow A\text{-}Sm_2O_3 + F$ was calculated as 2259 K according to the assumption.

ZrO_2–$GdO_{1.5}$ system

The calculated ZrO_2–$GdO_{1.5}$ phase diagram without considering the pyrochlore phase is shown in Fig. 6. Most of the experimental data are well consistent with the calculated phase diagram. The experimentally derived temperatures of [25] on the liquidus, and the reactions $L \leftrightarrow F + H\text{-}Gd_2O_3$ and $H\text{-}Gd_2O_3 \leftrightarrow F + B\text{-}Gd_2O_3$ are well reproduced, except the calculated solubility of $GdO_{1.5}$ in the fluorite phase for the reaction $L \leftrightarrow F + H\text{-}Gd_2O_3$, which is about 4 mol % larger and that for the reaction $H\text{-}Gd_2O_3 \leftrightarrow F + B\text{-}Gd_2O_3$, which is about 4 mol % less than the experimental data. The calculated phase compositions of the fluorite + $C\text{-}Gd_2O_3$ phase equilibrium shows good agreement with the experimental data of [32,33] and this work. The reaction $F + B\text{-}Gd_2O_3 \leftrightarrow C\text{-}Gd_2O_3$ is extrapolated to occur at 2275 K, which is thought to be reasonable. The solubility of ZrO_2 in C-type Gd_2O_3 reaches a maximum value near 1873 K, and decreases at higher temperatures. The composition of the fluorite phase of the invariant reactions reported by [25] were not fitted well because these data obtained by HTXRD could be less precise. The enthalpy of formation of the fluorite phase has to be increased in order to make a better fit for the phase compositions of the invariant reactions, while the agreement with the experimental data of the present work on both fluorite + $C\text{-}Gd_2O_3$ and fluorite + tetragonal phase equilibria would become worse.
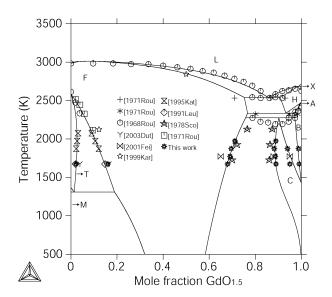

Fig. 6 Calculated ZrO_2–$GdO_{1.5}$ phase diagram without the pyrochlore phase compared with experimental data.

The calculated decomposition of the tetragonal phase into the monoclinic phase and fluorite occurs at 1309 K and 1.4 mol % $GdO_{1.5}$. The calculated phase boundaries for the fluorite + tetragonal equilibrium agree well with the experimental data of [30]. An enlarged phase diagram of the ZrO_2-rich side of the system together with the experimental data of the T_0 lines are shown in Fig. 7. The calculated T_0 temperatures against compositions are given by dashed lines. There is a difference of about 3 mol % $GdO_{1.5}$ difference between the T_0 data for tetragonal + fluorite equilibrium evaluated by [34] and the current calculation. A better fit would badly influence the phase diagram in other areas. The T_0
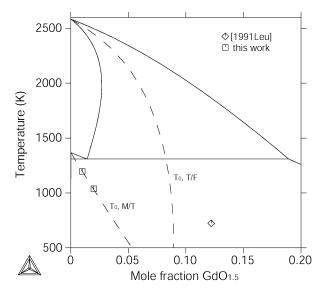
Fig. 7 Calculated partial ZrO_2–$GdO_{1.5}$ phase diagram and T_0 lines for the monoclinic + tetragonal and tetragonal + fluorite phase equilibria, together with the experimental data.

data obtained in this work by DTA measurement for the composition 1 and 2 mol % $GdO_{1.5}$ are plotted in Fig. 7, and the present calculation reproduces them well within the experimental uncertainty.

The calculated phase diagram using the order–disorder model for the pyrochlore phase is shown in Fig. 8. The second-order pyrochlore/fluorite phase transition boundary is denoted by a dashed line. The experimental data of [7] and this work are well reproduced. The data [35,36] are not considered due to their less reliability. In accordance with experimental data, a phase transition boundary symmetric to 50 mol % $GdO_{1.5}$ is obtained. At lower temperatures, the pyrochlore/fluorite phase boundary extends into the two-phase regions in both the ZrO_2- and $GdO_{1.5}$-rich region. It means at low temperatures the pyrochlore phase will be in equilibrium with both terminal solid solutions instead of the fluorite phase. The phase diagram modified in accordance with thermodynamic rules is shown in Fig. 9. At low temperatures, the phase boundaries of M + P and P + C-Gd_2O_3 two-phase equilibria are only slightly shifted, due to the small difference between the Gibbs energies of ordered pyrochlore and fluorite. It has to be mentioned that this phase diagram only gives the phase relations at the thermodynamically equilibrium state, and it doesn't mean that such two-phase regions occur under the condition of sluggish diffusion and the low driving force.

The site fractions of the Zr^{+4} and Gd^{+3} species in the first and second sublattices at the composition 50 mol % $GdO_{1.5}$ at different temperatures are calculated (Fig. 10). It can be seen that the completely ideal ordering only occurs at very low temperatures. With increasing the temperature, the ordering degree decreases gradually, and all the species fractions become identical at the temperature where the pyrochlore transforms into fluorite phase.
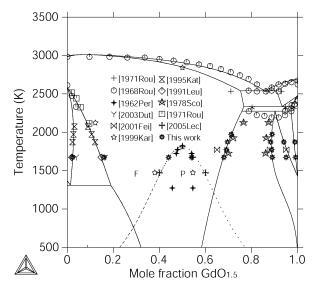
Fig. 8 Calculated ZrO_2–$GdO_{1.5}$ phase diagram including a second-order pyrochlore–fluorite transition boundary.
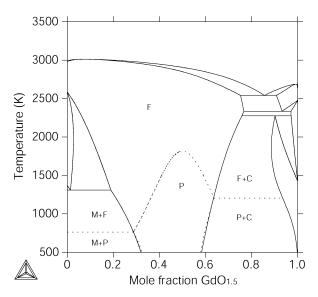

Fig. 9 Calculated ZrO_2–$GdO_{1.5}$ phase diagram modeled with a second-order pyrochlore–fluorite phase transition. The related phase boundaries are shown by dashed lines.
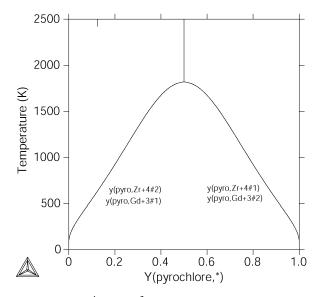
Fig. 10 Calculated site fractions of the Zr^{+4} and Gd^{+3} species in the first and second sublattices at the composition ZrO_2–50 mol % $GdO_{1.5}$ at different temperatures. With increasing temperature, the degree of order decreases.

ZrO_2–$DyO_{1.5}$ system

The calculated ZrO_2–$DyO_{1.5}$ phase diagram is shown in Fig. 11, together with the experimental data. The experimental phase boundary data obtained in this work and the liquidus data of [25] are well reproduced. A reasonable tetragonal + fluorite two-phase region is calculated based on the present experimental data. The XRD results of [37,38] show some deviation with this work, due to their lower accuracy. The calculated eutectoid point of the invariant reaction T ↔ F + M occurs at 1233 K and 3.2 mol % $DyO_{1.5}$. This temperature is much higher than the value 773 K reported by [37]. The present result is thought to be more reasonable, because the temperature of [37] obtained by dilatometry measurement is probably corresponding to the martensitic transformation temperature, rather than to the invariant reaction. Figure 12 presents the calculated T_0 lines for the monoclinic + tetragonal and tetragonal + fluorite equilibria, agreeing well with the experimental data obtained in this work.

The data on the fluorite + C-Dy_2O_3 phase equilibrium reported by [37,38] are not consistent with but are close to present calculations. With elevating the temperature, the solubility of ZrO_2 in C-type phase reduces in the temperature range studied. Two invariant reactions involving the C-type phase are calculated: H-Dy_2O_3 + F ↔ C-Dy_2O_3 at 2543 K and H-Dy_2O_3 ↔ B-Dy_2O_3 + C-Dy_2O_3 at 2445 K, for which the temperature is consistent with the experimental value 2423 K for this reaction reported by [25]. The temperature of the eutectic reaction L ↔ F + H-Dy_2O_3 calculated in this work is 2569 K, which is close to the experimental data 2543 K of [25], while the calculated composition of each phase shows large discrepancies with those reported by [25]. However, the temperature of the reaction H-Dy_2O_3 + F ↔ C-Dy_2O_3 predicted by the present calculation well reproduces the value of 2543 K for L ↔ F + H-Dy_2O_3 reported by [25]. In view of the large experimental uncertainties and the reliable fluorite + C-Dy_2O_3 phase equilibrium data obtained in this work, the results of the present calculations are accepted as more reasonable.
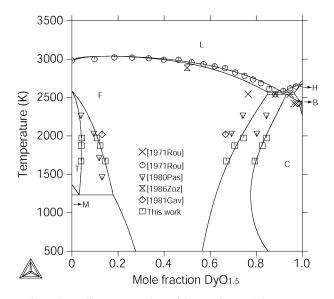
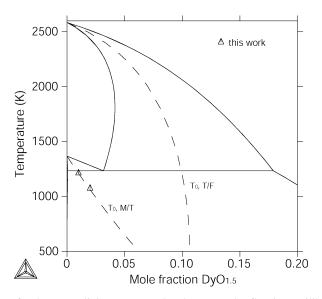**Fig. 11** Calculated ZrO_2–$DyO_{1.5}$ phase diagram together with experimental data.

Fig. 12 Calculated T_0 lines for the monoclinic + tetragonal and tetragonal + fluorite equilibria of the ZrO_2–$DyO_{1.5}$ system, together with experimental data.

ZrO_2–$YbO_{1.5}$ system

The calculated ZrO_2–$YbO_{1.5}$ phase diagram is shown in Fig. 13, together with the experimental data. The assessed tetragonal + fluorite two-phase region shows good agreement with the phase equilibria data obtained in this work and those data on the composition limits of the tetragonal phase by [39,40]. As for the fluorite phase, the data reported by [40] agree with current results well at high temperatures, and indicates discrepancy at low temperatures due to the experimental uncertainties. The phase boundary data of fluorite phase obtained in the work of [39] are less accurate, partly because the phase transformation character in this region is complicated so that XRD cannot correctly record the phase trans-
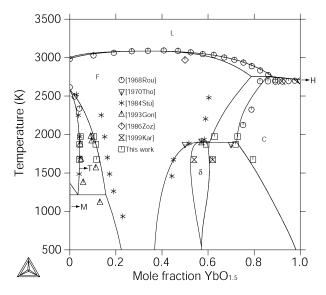
Fig. 13 Calculated ZrO_2–$YbO_{1.5}$ phase diagram together with experimental data.

formation temperatures. Likewise, the temperatures of decomposition of the tetragonal phase into fluorite and the monoclinic phase [39,40] seem to be too low compared to that of the equilibrium state. Presently, calculated eutectoid point of the invariant reaction T ↔ M + F is at 1215 K and 3.6 mol % $YbO_{1.5}$, while the related composition of the fluorite phase is 15.6 mol % $YbO_{1.5}$, and the solubility of $YbO_{1.5}$ in monoclinic phase is only around 0.1 mol %. The calculated liquidus show reasonable agreement with the experimental data considering their large uncertainties at such high temperatures. The congruent melting point of the fluorite phase calculated in this work is at 3085 K and 33.6 mol % $YbO_{1.5}$, which temperature is close to 3093 K reported by [25], but shows some discrepancy with respect to the composition (40 mol % $YbO_{1.5}$). Considering the smooth liquidus temperatures in a wide composition range and the large experimental uncertainties, the present calculated result is acceptable. At low temperatures, the experimental data on the F ↔ δ transition, and the invariant reaction F ↔ δ + C are also well reproduced. A symmetrical homogeneity range of the δ phase is assumed and finally obtained in the optimization, and is thought to be more reasonable than the nonsymmetrical one reported by [36]. For the reaction F ↔ δ + C, the calculated temperature is only 9 K lower than that of the F ↔ δ transformation, and presents considerable agreement with the experimental data reported by [39].

The solubility of ZrO_2 in C-type Yb_2O_3 reaches its maximum value at this invariant reaction, and decreases at elevated temperatures. The F/F + C-Yb_2O_3 phase boundary data of [39] show large discrepancy with the calculations and present experimental data. The literature data are less reliable because it is very difficult to study the F + C-Yb_2O_3 two-phase region only by XRD according to the experience gathered in the present work due to the overlapping of the XRD peaks of F and C-Yb_2O_3. In the Yb_2O_3-rich region, two calculated invariant reactions involving liquid phase are L ↔ C-Yb_2O_3 + H-Yb_2O_3 at 2717 K, and L + F ↔ C-Yb_2O_3 at 2754 K. In view of the large experimental uncertainties in this region, the present calculations provide at least a topologically reasonable phase diagram.

Figure 14 presents the calculated T_0 lines for the monoclinic + tetragonal and tetragonal + fluorite phase equilibria, in which the experimental T_0 data are well reproduced. However, the estimated T_0 data [41] for the transition between fluorite and T' do not agree well with the present calculation, since the calculation based on the equilibrium thermodynamics only gives the T_0 for the fluorite and tetragonal phase, and it is not clear yet if the Gibbs energy of metastable T' phase has exact the same be-
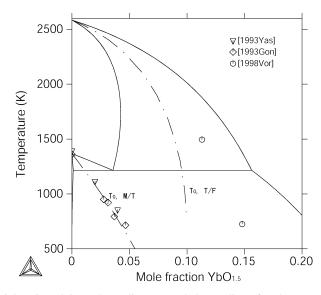
Fig. 14 Calculated partial ZrO_2–$YbO_{1.5}$ phase diagram and the T_0 lines for the monoclinic + tetragonal and tetragonal + fluorite phase equilibria, together with the experimental data.

havior as the stable tetragonal phase. Thus, a better fit with the experimental data is not necessary and will make the phase diagram worse.

CHARACTERISTIC CHANGES IN THE ZrO_2–$REO_{1.5}$ SYSTEMS

Evolutions of the phase relations in the ZrO_2–$REO_{1.5}$ systems

The RE oxides present similar physical and chemical properties, and show some trends with changing the ionic radius and molecular weight of the RE elements. As a matter of course, the phase relations in all the ZrO_2–$REO_{1.5}$ systems also reveal similar characteristics and evolve with the change of the ionic radius or molecular weight.

For each ZrO_2–$REO_{1.5}$ system except those with Dy and Sc, there is only one intermediate compound which is the ordered structure of the ZrO_2-based cubic fluorite-type phase. From La to Gd, the pyrochlore phase at stoichiometric composition (50 mol % $REO_{1.5}$) is the stable compound, and from Ho to Yb, the ordered structure is the δ phase with the stoichiometry of 57.14 mol % $REO_{1.5}$. In the case of Dy, no compound was found in this work. In the case of Sc, besides the δ phase, two other ordered compounds were also reported in literature [42,43]. Figure 15 collects the phase transition temperatures of the ordered phases in those systems. It is clear that the pyrochlore phase is preferably stable for the larger ionic radius of RE^{+3}, while the δ phase is preferably stable for the smaller ionic radius of RE^{+3}. With decreasing the ionic radius from La^{+3} to Dy^{+3} or increasing the ionic radius from Yb^{+3} to Dy^{+3}, both the pyrochlore and δ are less stable, and that is why no ordered compound is found in the ZrO_2–$DyO_{1.5}$ system. This is consistent with the fact that the pyrochlore is only stable when the $r_{A^{3+}}/r_{B^{4+}}$ ratio is between 1.46 and 1.80 [44]. On the other hand, even if the ordered structure can be thermodynamically stable, it will be kinetically very difficult to form at such low temperature.

As can be seen in Fig. 16, the solubility of $REO_{1.5}$ in tetragonal ZrO_2 increases when the ionic radius of RE reduces, and an approximate linear relation can be found for the solubility against ionic radius. At the same time, the fluorite phase field also extends towards lower solubility limits in the ZrO_2-rich region when the RE^{+3} has a smaller ionic radius. As a result, the width of the tetragonal + fluorite two-phase region becomes narrower with decreasing the ionic radius. Furthermore, the decom-
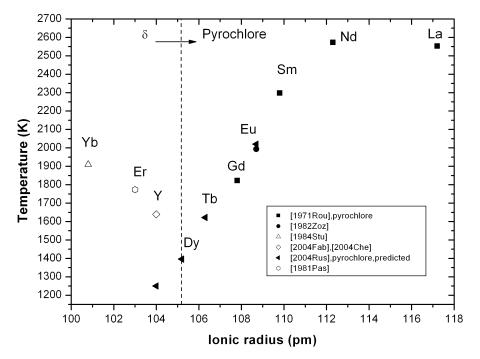
Fig. 15 Phase transformation temperatures of the ordered phases in the ZrO_2–$REO_{1.5}$ systems.
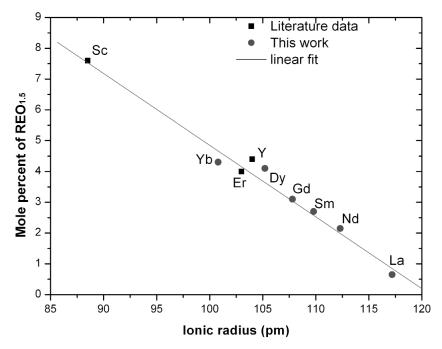

Fig. 16 Average solubility of $REO_{1.5}$ in tetragonal ZrO_2.

position temperature of the tetragonal phase (i.e,. T $\leftrightarrow$ F + M or T $\leftrightarrow$ P + M) is strongly influenced by the solubility limits of the tetragonal phase. Figure 17 shows the calculated ZrO_2-rich partial phase diagrams of the systems studied in this work without the pyrochlore phase. The clear trends for the change can be seen. Although some neighboring boundaries intersect each other in some temperature ranges, reasonable characteristic changes are given by the present calculations within the limits of uncertainties.
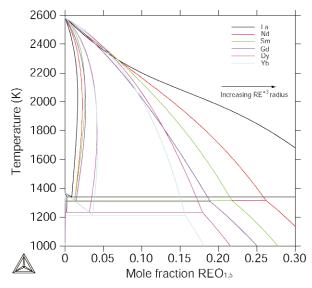

Fig. 17 Calculated ZrO_2-rich partial phase diagrams of different doping RE elements.

The linear functions of the lattice parameters of the fluorite phase constructed by Vegard's law for different systems are compiled in Fig. 18, in which the stable fluorite phase region at 1700 °C is lined out. With decreasing the lattice parameter of $REO_{1.5}$, some fluctuations are present on the width of the fluorite phase region due to the influence of the structural evolution of $REO_{1.5}$. The solubility of ZrO_2 in C-type $REO_{1.5}$ phase becomes larger when the radius of RE^{+3} decreases.

The phase equilibria are also related to the degree of lattice mismatch between different phases. According to the measured lattice parameters of the fluorite and pyrochlore phases in the ZrO_2–$NdO_{1.5}$, ZrO_2–$SmO_{1.5}$, and ZrO_2–$GdO_{1.5}$ systems, the interface between the disordered and ordered phases should be more coherent and have less lattice mismatch with decreasing the radius of RE^{+3}. This trend can be also applied to the equilibria between fluorite and the $REO_{1.5}$ terminal solution phase. The two phases in equilibrium form a narrower two-phase region when they are more coherent at interface. This is consistent with the XRD observations on the overlapping of the strong peaks of the fluorite and C-type phase in ZrO_2–$DyO_{1.5}$ and ZrO_2–$YbO_{1.5}$ systems. The large difference in SEM morphology between the two equilibrium phases (F + A equilibrium in the ZrO_2–$NdO_{1.5}$ system and F + B equilibrium in the ZrO_2–$SmO_{1.5}$ system) is also caused by the larger lattice mismatch for the case of larger RE^{+3}, while for the systems with F + C equilibrium and smaller RE^{+3}, the morphologies of fluorite and C-type phases do not show evident difference due to the more coherent interface.

At high temperatures, as it has been investigated by [25], the ZrO_2–$REO_{1.5}$ system with smaller ionic radius of RE^{+3} has higher temperatures of liquidus. At the same time, the temperatures for the invariant reactions involving liquid and fluorite phases in $REO_{1.5}$-rich side are also elevated.
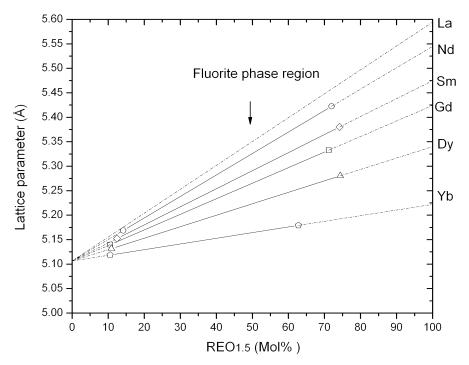
Fig. 18 Lattice parameters of fluorite phases in all ZrO_2–$REO_{1.5}$ systems constructed by Vegard's law (the solid lines give the stable fluorite phase region at 1700 °C).

Evolutions of the thermodynamic properties in the ZrO_2–$REO_{1.5}$ systems

The phase relations are definitely determined by the thermodynamic properties of phases. With the change of the ionic radius of RE^{+3}, it is found and confirmed in this work that some thermodynamic properties of different phases change towards a single trend.

Figure 19 presents the enthalpy of formation of fluorite and pyrochlore phases, which are the most important thermodynamic data for ZrO_2–$REO_{1.5}$ systems. The experimental data of [45] indicate that both fluorite and pyrochlore phases are more stable with decreasing the ionic radius of RE^{+3}. The experimental data reported by [46–48] are shown together with the fitted blue line, and it is interesting that all the data hold a single linear function, so that the fluorite phase in the system with smaller RE^{+3} ionic radius is less stable. Present calculated results are given by the red symbols, in which the values for the pyrochlore phases are consistent with those of [48] within the experimental limits. However, present calculations on the enthalpies of formation of fluorite phases show complete different trends from those of [45–47]. With decreasing the RE^{+3} ionic radius, the enthalpy of formation of fluorite phase becomes more negative. This is consistent with the phase relations that the tetragonal + fluorite two-phase region becomes gradually narrower with decreasing the radius of RE^{+3}. Moreover, it can be seen from Fig. 19 that the difference between the enthalpies of fluorite and pyrochlore becomes gradually larger with increasing the radius of RE^{+3}, and this tendency also agrees with the phase diagram that in case of a larger ionic radius of RE^{+3} there is a wider fluorite + pyrochlore two-phase region, which is corresponding to larger difference between the Gibbs energies of fluorite and pyrochlore phases. Therefore, in view of those agreements with the evolution of phase relations, the present calculations on the enthalpies of formation of fluorite and pyrochlore are undoubtedly more reasonable than those experimental data.
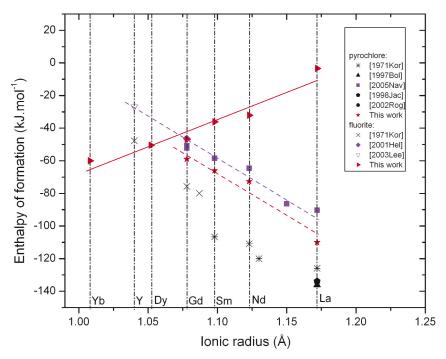
Fig. 19 Experimental and calculated enthalpies of formation of pyrochlore and fluorite (per four moles of cations, reference state: the monoclinic ZrO_2 and the stable structure of $REO_{1.5}$ at room temperature, for the composition at 50 mol % $REO_{1.5}$).

From La to Yb, the stable structure of RE oxides at ambient temperature changes from A- to C-type. With the change of the ionic radius of RE^{+3}, the enthalpies of transformation between those stable structures at ambient temperature to metastable fluorite structure are plotted in Fig. 20 together with the experimental and extrapolated data on the ZrO_2–$YO_{1.5}$ system. Following the energetic trends established for the structural transformations among the A, B, C, H and X-type structures [19], present calculations show the increasing values on the enthalpy of the A → F or C → F transformation towards the larger ionic radius of RE^{+3}, and the linear functions can be constructed accordingly. So far, there is no reliable reference data on the enthalpy or entropy of those transformations for any system. Because such data cannot be obtained directly from experiments, some assumptions had to be made in the present work.

For the corresponding entropies of transformation, it was assumed that those of C → F for RE = Sm, Gd, Dy are identical, and so do those of A → F for RE = La, Nd. However, for the transformation C → F, when RE = Yb, a lower entropy was selected during optimization. Figure 21 shows an approximate increasing trend of the entropies against the ionic radius. Further experimental investigations are necessary to confirm the trends found in present calculations.
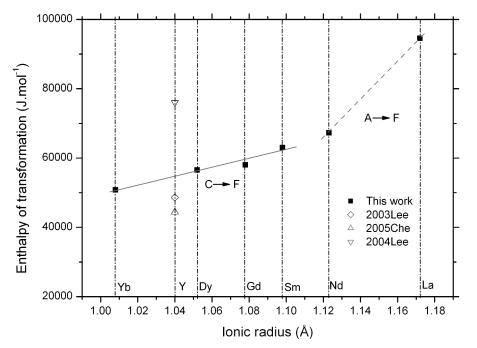
Fig. 20 Calculated enthalpies of the A → F (RE = La, Nd) and C → F (RE = Sm, Gd, Dy, Y, Yb) transformations in RE_2O_3 compounds.

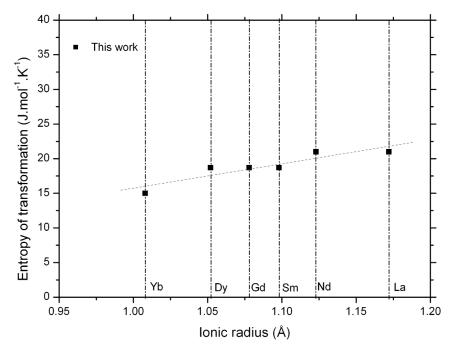**Fig. 21** Calculated entropies of the A → F (RE = La, Nd) and C → F (RE = Sm, Gd, Dy, Yb) transformations in RE_2O_3 compounds.

REFERENCES

1. C. G. Levi. *Curr. Opin. Solid State Mater. Sci.* **8**, 77 (2004).
2. J. R. Nicholls, K. J. Lawson, A. Johnstone, D. S. Rickerby. *Surf. Coat. Technol.* **151–152**, 383 (2002).
3. D. Zhu, Y. L. Chen, R. A. Miller. *Ceram. Eng. Sci. Proc.* **24**, 525 (2003).
4. R. Vassen, X. Q. Cao, F. Tietz, D. Basu, D. Stöver. *J. Am. Ceram. Soc.* **83**, 2023 (2000).
5. J. Wu, X. Wei, N. P. Padture, P. G. Klemens, M. Gell, E. Garcia, P. Miranzo, M. I. Osendi. *J. Am. Ceram. Soc.* **85**, 3031 (2002).
6. M. J. Maloney. U.S. Patent 6 177 200 (2001).
7. R. M. Leckie, S. Kraemer, M. Ruhle, C. G. Levi. *Acta Mater.* **53**, 3281 (2005).
8. Chong Wang. PhD. Thesis, University of Stuttgart (2006).
9. E. C. Subbarao, H. S. Maiti, K. K. Srivastava. *Phys. Status Solidi A* **21**, 9 (1974).
10. E. R. Andrievsakaya, L. M. Lopato. *J. Mater. Sci.* **30**, 2591 (1995).
11. M. Yashima, T. Mitsuhashi, H. Takashina, M. Kakihana, T. Ikegami, M. Yoshimura. *J. Am. Ceram. Soc.* **78**, 2225 (1995).
12. T. S. Sheu, T. Y. Tien, I. W. Chen. *J. Am. Ceram. Soc.* **75**, 1108 (1992).
13. M. Yashima, M. Kakihana, M. Yoshimura. *Solid State Ionics* **86–88**, 1131 (1996).
14. V. Lughi, D. R. Clarke. *Surf. Coat. Technol.* **200**, 1287 (2005).
15. O. Fabrichnaya, F. Aldinger. *Z. Metallkd.* **95**, 27 (2004).
16. S. Lakiza, O. Fabrichnaya, Ch. Wang, M. Zinkevich, F. Aldinger. *J. Eur. Ceram. Soc.* **26**, 233 (2006).
17. M. Hillert. *J. Alloy. Compd.* **320**, 161 (2001).
18. O. Redlich, A. T. Kister. *Ind. Eng. Chem.* **40**, 345 (1948).
19. M. Zinkevich. *Prog. Mater. Sci.* **52**, 597 (2007).
20. L. Minervini, R. W. Grimes, K. E. Sickafus. *J. Am. Ceram. Soc.* **83**, 1873 (2000).
21. C. R. Stanek, L. Minervini, R. W. Grimes. *J. Am. Ceram. Soc.* **85**, 2792 (2002).
22. V. P. Red'ko, L. M. Lopato. *Inorg. Mater.* **27**, 1609 (1991).
23. H. J. Rossell. *J. Solid State Chem.* **19**, 103 (1976).
24. A. Rouanet. *C. R. Acad. Sci. Paris Series C* **267**, 395 (1968).
25. A. Rouanet. *Rev. Int. Hautes Temp. Refract.* **8**, 161 (1971).
26. S. M. Lakiza, L. M. Lopato. *J. Eur. Ceram. Soc.* **25**, 1373 (2005).
27. H. M. Ondik (Ed.). In *Phase Diagrams for Zirconium and Zirconia Systems*, National Institute of Standards and Technology, Gaithersburg, MD (1998).
28. B. Bastide, P. Odier, J. P. Coutures. *J. Am. Ceram. Soc.* **71**, 449 (1988).
29. M. Yashima, N. Ishizawa, T. Noma, M. Yoshimura. *J. Ceram. Soc. Japan* **101**, 871 (1993).
30. J. Katamura, T. Seri, T. Sakuma. *J. Phase Equilib.* **16**, 315 (1995).
31. Y. Tabira, R. L. Withers. *J. Solid State Chem.* **148**, 205 (1999).
32. H. G. Scott. *J. Mater. Sci.* **13**, 1592 (1978).
33. A. J. Feighery, J. T. S. Irvine, C. Zheng. *J. Solid State Chem.* **160**, 302 (2001).
34. D. K. Leung, C. J. Chan, M. Rühle, F. Lange. *J. Am. Ceram. Soc.* **74**, 2786 (1991).
35. M. Perez Y Jorba. *Ann. Chim.* **7**, 479 (1962).
36. A. G. Karaulov, E. I. Zoz. *Refract. Ind. Ceram.* **40**, 479 (1999).
37. C. Pascual, P. Duran. *J. Mater. Sci.* **15**, 1701 (1980).
38. A. M. Gavrish, L. S. Alekseenko, L. A. Tarasova, G. P. Orekhova. *Inorg. Mater.* **17**, 1541 (1981).
39. V. S. Stubican, G. S. Corman, J. R. Hellmann, G. Senft. In *Advances in Ceramics*, Science and Technology of Zirconia II, Vol. 12, N. Claussen, M. Rühle, A. H. Heuer (Eds.), pp. 96–106, The American Ceramic Society, Columbus, OH (1984).
40. M. Gonzalez, C. Moure, J. R. Jurado, P. Duran. *J. Mater. Sci.* **28**, 3451 (1993).
41. Yu. K. Voron'ko, A. A. Sobol', L. I. Tsymbal. *Inorg. Mater.* **34**, 350 (1998).

42. M. Spiridonov, L. N. Popova, R. Ya. Popil'skii. *J. Solid State Chem.* **2**, 430 (1970).
43. M. R. Thornber, D. J. M. Bevan, E. Summerville. *J. Solid State Chem.* **1**, 545 (1970).
44. M. A. Subramanian, G. Aravamudan, G. V. Subba Rao. *Prog. Solid State Chem.* **15**, 55 (1983).
45. V. R. Korneev, V. B. Glushkova, E. K. Keler. *Inorg. Mater.* **7**, 781 (1971).
46. K. Helean, B. D. Begg, A. Navrotsky, B. Ebbinghaus, W. J. Weber, R. C. Ewing. *Mater. Res. Soc. Symp. Proc.* **663**, 691 (2001).
47. T. A. Lee, A. Navrotsky, I. Molodetsky. *J. Mater. Res.* **18**, 908 (2003).
48. A. Navrotsky. *J. Mater. Chem.* **15**, 1883 (2005).